Supplementary Materials for

Laterally varying crustal and Quaternary fault-zone structures in the Seoul metropolitan area, South Korea from a joint inversion analysis based on dense seismic arrays

Jeongin Lee[1], Tae-Kyung Hong[1*], Seongjun Park[1], Junhyung Lee[1], Dongchan Chung[1], and Byeongwoo Kim[1]

Affiliation and address:

[1]Yonsei University, Department of Earth System Sciences, 50 Yonsei-ro, Seodaemun-gu Seoul 03722, South Korea.

Correspondence to:

tkhong@yonsei.ac.kr (Tae-Kyung Hong)

Contents of this file

Introduction

The supplementary materials provide information on the method and additional results.

Event information

We present the information of earthquakes used for teleseismic receiver function analysis in Table S1, local surface-wave dispersion analysis in Table S2, and regional surface-wave dispersion analysis in Table S3.

Method

Receiver function analysis

The arrival time differences between the P waves and P-to-S waves provide information on the layer interfaces. Near-source and travel path effects are corrected (Langston, 1979; Ammon et al., 1990). We apply an equalization procedure to deconvolve the instrument responses and source time functions from the observed waveforms (Langston, 1979). The equalization procedure deconvolves the vertical P waveforms from the radial wavetrains, yielding the receiver functions. We use a time-domain iterative deconvolution method to search an optimum receiver function that yields the minimum misfit error between the observed radial seismograms and synthetic receiver functions convolved with vertical P waves (Kikuchi and Kanamori, 1982; Ligorria and Ammon, 1999).

We prepare radial and vertical waveforms that are filtered using a Gaussian filter. The

Gaussian filter is given by

$$H(f) = \exp\left[-\left(\frac{\pi f}{\alpha_1}\right)^2\right], \tag{S1}$$

where f is the frequency, and α_1 is the bandwidth constant. We determine the time lags of spikes in the radial wavetrains by cross-correlating with vertical P waveforms (Ligorria and Ammon, 1999):

$$r_h(t') = \int_0^\infty z(t)\, h(t + t')\, dt, \tag{S2}$$

where $r_h(t)$ is the cross-correlation function in time t, $z(t)$ is the observed vertical P waveforms, and $h(t)$ is the observed radial waveforms. The spike amplitudes are determined by

$$R_a(t) = \frac{r_h(t)}{r_z(t)}, \tag{S3}$$

where $R_a(t)$ is the receiver function amplitude at time t, and $r_z(t)$ is the autocorrelation function of vertical P waveforms. zz We calculate synthetic radial waveforms by superposing the vertical P waveforms convolved with spikes of amplitudes (Kikuchi and Kanamori, 1982; Wang and Pavlis, 2016):

$$y(t) = \sum_{l=1}^{N_s} R_a(t_l)\ \{z(t) * \delta(t - t_l)\}, \tag{S4}$$

where $y(t)$ is the synthetic radial waveforms at time t, N_s is the number of spikes, $z(t)$ is the vertical P waveforms, and t_l is the lag time of lth spike. Here, the spikes are ordered by the spike amplitudes. We iterative search the optimal number of spikes until the misfit error between the observed and synthetic radial waveforms is sufficiently small. The misfit error is determined by

$$\Delta_h = \int_0^\infty [h(t) - y(t)]^2 dt, \tag{S5}$$

where $h(t)$ is the observed radial waveforms at time t, and $y(t)$ is the synthetic radial waveforms.

For receiver function analysis, we collected seismic waveforms for 156 earthquakes with epicentral distances of 30°-90°. The teleseismic event information used in the study is presented in Table S1.

Surface-wave dispersion analysis

We estimate the dispersion curves of fundamental-mode Rayleigh wave using a multiple filter technique (MFT) (Dziwonski et al., 1969; Herrmann, 1973). The multiple filter technique determines the group velocity of a dispersed wave using a narrow Gaussian filter. The dispersive waves at time t and distance r can be expressed by (Herrmann, 1973)

$$g(t,r) = \frac{1}{2\pi} \int_{\omega_0-\omega_c}^{\omega_0+\omega_c} H(\omega,\omega_0) A(\omega,r) \exp[i(\omega t - kr)]\, d\omega, \tag{S6}$$

where ω is the angular frequency of waves, k is the wavenumber, A is the complex amplitude, $H(\omega,\omega_0)$ is a symmetric bandpass filter function with center frequency ω_0, and ω_c is the half width of cutoff frequencies. The Gaussian filter function is given by

$$H(\omega,\omega_0) = \exp\left[-\frac{\alpha_2\,(\omega-\omega_0)^2}{\omega_0^2}\right], \tag{S7}$$

where α_2 is a distance-dependent filter parameter.

The filtered dispersed wave of a single mode is given by (Herrmann, 1973)

$$g(t,r) = \frac{A\omega_0}{2\pi}\sqrt{\frac{\pi}{\alpha}} \exp[i(\omega_0 t - k_0 r)] \exp\left[-\frac{\omega_0^2}{4\alpha}\left(t-\frac{r}{U_0}\right)^2\right], \tag{S8}$$

where t is the time, r is the distance, U_0 is the group velocity, A is a constant. The envelope of $g(t,r)$ has a peak value at time $t = r/U_0$. We determine the envelope maxima of each mode. The individual envelop maxima suggests the mode arrival time (Herrmann, 1973).

Theoretical surface-wave dispersion curves are calculated using the Schwab-Knopoff method that is based on the Thomson-Haskell technique for layered media (Thomson, 1950; Haskell, 1953; Schwab and Knopoff, 1970). A best-fit velocity model to yield the minimum residuals between the observed and theoretical dispersion curves is searched for the model inversion.

We used 14 local earthquakes and 17 regional earthquakes to obtain surface wave group velocity dispersion. The local and regional event information used in the study is presented in Tables S2 and S3.

Joint inversion

We determine the S-wave velocity model using an iterative least-squares inversion method (Özalaybey et al., 1997; Du and Foulger, 1999; Julià et al., 2000). The parameters (seismic velocities in layers) of the model with fixed layer thickness are iteratively searched to minimize the joint prediction error that assesses the residuals between observed and theoretical receiver functions and dispersion curves.

The joint prediction error, E, is defined as (Julià et al., 2000):

$$E = \frac{1-\gamma}{N_r} \sum_{i=0}^{N_r} \left(\frac{r(t_i)|_{obs} - r(t_i)|_{pre}}{\sigma_i} \right)^2 + \frac{\gamma}{N_s} \sum_{j=0}^{N_s} \left(\frac{d_j|_{obs} - d_j|_{pre}}{\sigma_j} \right)^2, \tag{S9}$$

where S is the minimum, $r(t_i)|_{obs}$ is the observed receiver function at time t_i, $r(t_i)|_{pre}$ is the predicted receiver function at time t_i, σ_i is the corresponding standard deviation of receiver function data set, $d_j|_{obs}$ is the observed jth surface wave dispersion, $d_j|_{pre}$ is the predicted jth surface wave dispersion, σ_j is the standard deviation of the jth surface wave dispersion data set, N_r is the number of receiver function data, N_d is the number of surface wave dispersion data, and γ is the influence factor ($0 \leq \gamma \leq 1$). Here, velocity models are inverted based only on the surface-wave dispersion analysis when γ=1. On the other hand, velocity models are entirely dependent on the receiver function analysis when γ=0.

We assign a positive damping factor η to avoid unrealistic highly-fluctuating velocities during inversion (Julià et al., 2000). Also, we determine the medium density using an empirical relationship with P-wave velocity (Berteussen, 1977):

$$\rho = 0.32\, V_P + 0.77, \tag{S10}$$

where ρ is the medium density in g/cm^3, and V_P is the P-wave velocity in km/s. Here, the P-wave velocity is determined assuming a Poisson solid.

H-κ analysis

We determine the Moho depth (crustal thickness, H) and V_P/V_S ratio (κ) using the arrival times of P-to-S converted waves on the Moho (Zhu and Kanamori, 2000; Nair et al., 2006).

We stack weighted receiver-function amplitudes of three phases (Zhu and Kanamori, 2000):

$$s(H,\kappa) = w_1 r(t_1) + w_2 r(t_2) + w_3 r(t_3), \tag{S11}$$

where w_i is the priori weight at time t_i, $r(t_i)$ is the receiver function at time t_i, t_1 is the arrival time of phase *Ps*, t_2 is the arrival time of phase *PpPs*, and t_3 is the arrival time of phase *PsPs+PpSs* (Zhu and Kanamori, 2000). We search optimal values of crustal thickness and V_P/V_S ratio that maximize $s(H,k)$.

Additional results

The joint inversion analysis is performed with a homogeneous half-space initial model (Fig. S1). The joint inversion yields the results stably with the change of initial models. The surface-wave dispersion curves used for the joint inversion analysis. The observed surface-wave dispersion curves are compared with theoretical surface-wave dispersion curves based on inverted velocity models from joint inversion analysis (Fig. S2). Joint inversion analysis with the influence factor of 0.5 yields velocity models that produce theoretical dispersion curves to match with the observed dispersion curves. Also, the observed receiver function profiles match with the theoretical arrival times (Fig. S3).

The accuracy tests of joint inversion analysis with influence factor of 0.5 are presented (Fig. S5). The joint inversion analysis with influence factor of 0.5 yield relatively vertically smoothed models. Receiver function profiles from joint inversions analyses with different influence factors (0.15, 0.5) are compared with observed receiver function profiles for Gaussian filter parameters (α_1) of 1.0 and 2.5 (Figs. S5, S6). The synthetic receiver function profiles match well with the observed receiver function profiles for both influence factors (0.15, 0.5). The minimum number of data points is 11 which is large enough to ensure stable results (Fig. S7). A bootstrap test supports the stability of analysis.

The vertical structures of four subregions are additionally calculated using joint inversion analysis with influence factor of 0.5 and conventional receiver function analysis (Figs. S8, S9). Both inversions produce similar structures. The vertical structures from joint inversion analysis with influence factor of 0.5 produce vertically smoothed structures, while those from conventional receiver function analysis yields relatively large perturbations. Similar features are observed in the velocity structures along three profiles across Seoul (Figs. S10, S11), lateral shear-wave velocity models for the Seoul metropolitan area (Figs. S12, S13), lateral shear-wave velocity models for city Seoul (Figs. S14, S15), and vertical crosssections (Figs. S16, S17).

References

Ammon, C. J., Randall, G. E., and Zandt, G. (1990), On the nonuniqueness of receiver function inversions, Journal of Geophysical Research: Solid Earth, 95 (B10), 15303-15318.

Berteussen, K. A. (1977), Moho depth determinations based on spectral-ratio analysis of NORSAR long-period P waves, Physics of the Earth and Planetary Interiors, 15 (1), 13-27.

Du, Z. J., and G. R. Foulger (1999), The crustal structure beneath the northwest fjords, Iceland, from receiver functions and surface waves, Geophysical Journal International, 139 (2), 419-432.

Dziewonski, A. M., A. Block, and M. Landisman (1969), A technique for the analysis of transient seismic signals, Bulletin of the Seismological Society of America, 59 (1), 427-444.

Haskell, N. A. (1953), The dispersion of surface waves on multilayered media, Bulletin of the seismological Society of America, 43 (1), 17-34.

Herrmann, R. B. (1973), Some aspects of band-pass filtering of surface waves, Bulletin of the Seismological Society of America, 63 (2), 663-671.

Julià, J., Ammon, C. J., Herrmann, R. B., and Correig, A. M. (2000), Joint inversion of receiver function and surface wave dispersion observations, Geophysical Journal International, 143 (1), 99-112.

Kikuchi, M., and Kanamori, H. (1982), Inversion of complex body waves, Bulletin of the Seismological Society of America, 72 (2), 491-506.

Langston, C. A. (1979), Structure under Mount Rainier, Washington, inferred from teleseismic body waves, Journal of Geophysical Research, 84 (B9), 4749-4762.

Ligorría, J. P., and C. J. Ammon (1999), Iterative deconvolution of teleseismic seismograms and receiver function estimation, Bulletin of the Seismological Society of America, 89 (5), 1395-1400.

Nair, S. K., Gao, S. S., Liu, K. H., and Silver, P. G. (2006), Southern African crustal evolution and composition: Constraints from receiver function studies, Journal of Geophysical Research: Solid Earth, 111, B02304, https://doi.org/10.1029/2005JB003802.

Özalaybey, S., Savage, M. K., Sheehan, A. F., Louie, J. N., and Brune, J. N. (1997), Shear-wave velocity structure in the northern Basin and Range province from the combined analysis of receiver functions and surface waves, Bulletin of the Seismological Society of America, 87 (1), 183-199.

Schwab, F., and L. Knopoff (1970), Surface-wave dispersion computations, Bulletin of the Seismological Society of America, 60 (2), 321-344.

Thomson, W. T. (1950), Transmission of elastic waves through a stratified solid medium, Journal of Applied Physics, 21 (2), 89-93.

Wang, Y., and Pavlis, G. L. (2016), Generalized iterative deconvolution for receiver function estimation, Geophysical Journal International, 204 (2), 1086-1099.

Zhu, L., and Kanamori, H. (2000), Moho depth variation in southern California from teleseismic receiver functions. Journal of Geophysical Research: Solid Earth, 105 (B2), 2969-2980.

Table S1. Teleseismic earthquakes used for receiver function analysis. The event origin times, locations, focal depths, magnitudes (M_W), and numbers of stations (N_s) used for the analysis are presented.

No	date (yyyy/mm/dd)	time (hh:mm:ss)	lat (°N)	lon (°E)	dep (km)	M_W	N_s
1	2015/07/10	04:12:42	-9.354	158.342	20.0	6.7	2
2	2015/07/18	02:27:32	-10.457	165.101	11.8	6.9	3
3	2015/07/27	04:49:45	52.276	-169.535	27.8	6.9	1
4	2015/07/27	21:41:20	-2.713	138.543	47.8	7	3
5	2015/08/10	04:12:14	-9.284	158.027	20.0	6.6	3
6	2015/08/12	18:49:24	-9.307	157.821	11.3	6.5	1
7	2015/09/24	15:53:27	-0.620	131.260	18.0	6.6	3
8	2015/10/20	21:52:02	-14.860	167.303	135.0	7.1	3
9	2015/10/26	09:09:42	36.524	70.368	231.0	7.5	2
10	2015/11/04	03:44:15	-8.338	124.875	20.0	6.5	2
11	2015/11/18	18:31:04	-8.899	158.422	12.6	6.8	2
12	2015/12/07	07:50:05	38.211	72.780	22.0	7.2	2
13	2015/12/09	10:21:48	-4.106	129.508	21.0	6.9	3
14	2016/01/30	03:25:10	54.006	158.513	163.2	7.2	2
15	2016/03/20	22:50:20	54.294	162.813	30.0	6.4	1
16	2016/04/06	06:58:48	-14.068	166.625	24.0	6.7	2
17	2016/04/10	10:28:58	36.473	71.131	212.0	6.6	3
18	2016/04/13	13:55:17	23.094	94.865	136.0	6.9	2
19	2016/04/28	19:33:24	-16.043	167.379	24.0	7	3
20	2016/05/28	05:38:50	-21.972	-178.204	405.7	6.9	2
21	2016/08/12	01:26:36	-22.478	173.111	16.4	7.2	3
22	2016/08/24	01:36:32	42.723	13.188	4.4	6.2	1
23	2016/08/24	10:34:54	20.922	94.569	82.0	6.8	2
24	2016/10/17	06:14:58	-6.053	148.862	35.0	6.9	3
25	2016/10/30	06:40:19	42.855	13.088	10.0	6.6	1
26	2016/11/13	11:02:59	-42.725	173.065	22.0	7.8	2
27	2016/11/25	14:24:30	39.230	74.021	17.0	6.6	2
28	2016/12/06	22:03:33	5.283	96.168	13.0	6.5	1

Table S1. *(continued)*

No	date (yyyy/mm/dd)	time (hh:mm:ss)	lat (°N)	lon (°E)	dep (km)	M_W	N_s
29	2016/12/08	17:38:46	-10.676	161.330	41.0	7.8	3
30	2016/12/09	19:10:07	-10.748	161.123	21.1	6.9	2
31	2016/12/17	10:51:10	-4.505	153.522	94.5	7.9	3
32	2016/12/21	00:17:14	-7.508	127.921	152.0	6.7	2
33	2017/01/03	21:52:30	-19.354	176.058	12.0	6.9	2
34	2017/01/10	06:13:47	4.463	122.575	612.7	7.3	1
35	2017/01/19	23:04:21	-10.343	161.318	36.0	6.5	1
36	2017/01/22	04:30:22	-6.215	155.144	135.0	7.9	3
37	2017/11/01	02:23:55	-21.669	168.888	9.9	6.6	1
38	2017/11/04	09:00:19	-15.320	-173.168	10.0	6.8	1
39	2017/11/07	21:26:38	-4.243	143.485	110.6	6.5	1
40	2017/11/19	22:43:29	-21.334	168.683	10.0	7	1
41	2018/01/23	09:31:42	56.046	-149.073	25.0	7.9	5
42	2018/01/26	22:47:57	-3.514	145.848	10.0	6.3	2
43	2018/02/25	17:44:44	-6.053	142.770	24.4	7.5	12
44	2018/02/26	13:34:53	-2.763	126.727	9.9	6.1	4
45	2018/02/26	15:18:00	-6.505	143.255	19.0	6.3	4
46	2018/02/28	02:45:45	-6.167	142.480	16.0	6.1	7
47	2018/03/06	14:13:06	-6.293	142.613	10.0	6.7	7
48	2018/03/08	17:39:51	-4.385	153.187	22.5	6.8	9
49	2018/03/24	11:23:32	-5.496	151.497	33.0	6.3	8
50	2018/03/25	20:14:47	-6.625	129.814	169.0	6.4	9
51	2018/03/26	09:51:00	-5.462	151.396	40.0	6.6	4
52	2018/03/26	09:51:00	-5.462	151.396	40.0	6.6	6
53	2018/03/29	21:25:36	-5.495	151.507	35.0	6.9	8
54	2018/04/02	05:57:31	-24.897	-176.606	83.5	6.1	2
55	2018/05/04	22:32:54	19.313	-154.998	2.1	6.9	2
56	2018/05/09	10:41:45	36.992	71.383	116.0	6.2	8

Table S1. *(continued)*

No	date (yyyy/mm/dd)	time (hh:mm:ss)	lat (°N)	lon (°E)	dep (km)	M_W	N_s
57	2018/06/21	21:13:32	-17.796	168.056	28.0	6.1	5
58	2018/07/13	09:46:49	-18.933	169.022	169.2	6.4	6
59	2018/07/28	22:47:38	-8.240	116.508	14.0	6.4	12
60	2018/08/05	11:46:38	-8.260	116.436	31.0	6.9	8
61	2018/08/15	21:56:54	51.422	-178.052	20.0	6.6	8
62	2018/08/19	00:19:40	-18.113	-178.154	600.0	8.2	11
63	2018/08/19	14:56:28	-8.330	116.631	25.2	6.9	11
64	2018/08/29	03:51:56	-22.066	170.050	26.7	7.1	5
65	2018/09/06	15:49:14	-18.495	179.356	617.9	7.9	8
66	2018/09/09	19:31:35	-10.021	161.503	68.0	6.5	7
67	2018/09/10	04:19:02	-31.745	-179.373	115.0	6.9	11
68	2018/09/28	10:02:43	-0.178	119.840	10.0	7.5	12
69	2018/10/10	18:44:55	-7.453	114.456	9.0	6	6
70	2018/10/10	20:48:20	-5.708	151.220	45.1	7	22
71	2018/10/25	22:54:52	37.515	20.564	14.0	6.8	2
72	2018/11/16	03:26:55	-10.549	163.158	8.8	6.1	2
73	2018/11/18	20:25:46	-17.874	-178.927	540.0	6.8	2
74	2018/11/30	17:29:29	61.346	-149.955	46.7	7	21
75	2018/12/01	13:27:21	-7.384	128.707	136.0	6.4	23
76	2018/12/05	04:18:08	-21.957	169.418	10.0	7.5	24
77	2018/12/05	06:43:04	-22.050	169.668	10.0	6.6	4
78	2018/12/16	09:42:37	-3.923	140.232	62.0	6.1	6
79	2018/12/20	17:01:55	55.100	164.699	16.6	7.3	21
80	2018/12/22	14:25:01	-13.394	166.812	42.0	6	3
81	2018/12/23	23:08:43	-20.287	-175.092	113.0	6.4	1
82	2018/12/29	03:39:09	5.898	126.921	60.2	7	20
83	2018/12/29	03:39:09	5.898	126.921	60.2	7	1
84	2018/12/31	02:35:37	54.427	-161.513	31.0	6	4

Table S1. *(continued)*

No	date (yyyy/mm/dd)	time (hh:mm:ss)	lat (°N)	lon (°E)	dep (km)	M_W	N_s
85	2019/01/06	17:27:20	2.241	126.736	60.0	6.6	19
86	2019/01/15	18:06:34	-13.331	166.879	35.0	6.6	10
87	2019/01/18	13:18:32	-19.208	168.633	45.1	6	1
88	2019/01/21	23:59:22	-10.311	119.147	16.8	6	7
89	2019/01/22	05:10:03	-10.466	119.031	27.0	6.4	19
90	2019/03/10	12:48:03	-10.140	152.055	30.0	6.1	1
91	2019/03/20	15:23:58	-15.597	167.655	119.0	6.3	1
92	2019/03/24	04:37:35	1.662	126.380	45.0	6.1	6
93	2019/04/06	21:55:01	-6.849	125.014	539.0	6.3	22
94	2019/04/12	11:40:49	-1.852	122.553	17.5	6.8	16
95	2019/05/14	12:58:26	-4.081	152.569	10.0	7.5	24
96	2019/05/23	08:45:17	51.308	-178.239	30.0	6.1	7
97	2019/05/31	10:12:32	6.264	126.552	90.2	6.1	7
98	2019/06/15	22:55:04	-30.644	-178.106	46.0	7.3	34
99	2019/06/19	17:24:48	-2.243	138.460	10.0	6.3	39
100	2019/06/24	01:05:29	-2.776	138.568	28.0	6.1	37
101	2019/06/24	02:53:39	-6.408	129.169	212.0	7.3	41
102	2019/07/07	15:08:40	0.513	126.189	35.0	6.9	40
103	2019/07/14	05:39:23	-18.224	120.357	10.0	6.6	38
104	2019/07/14	09:10:50	-0.529	128.093	10.0	7.3	39
105	2019/07/15	08:21:35	-5.990	149.552	59.0	6.2	30
106	2019/07/31	15:02:33	-16.199	167.998	181.0	6.6	20
107	2019/08/02	12:03:27	-7.267	104.825	52.8	6.9	31
108	2019/08/24	15:51:27	-14.290	167.198	115.0	6	14
109	2019/09/01	15:54:20	-20.360	-178.567	591.0	6.6	6
110	2019/09/25	23:46:43	-3.460	128.368	9.0	6.5	27
111	2019/09/29	02:02:51	5.693	126.550	73.0	6.2	28
112	2019/10/16	11:37:05	6.714	125.001	12.8	6.4	3

Table S1. *(continued)*

No	date (yyyy/mm/dd)	time (hh:mm:ss)	lat (°N)	lon (°E)	dep (km)	M_W	N_s
113	2019/10/21	02:52:29	-19.018	169.488	231.0	6.4	20
114	2019/10/29	01:04:43	6.759	124.995	15.0	6.6	27
115	2019/10/31	01:11:19	6.908	125.183	10.0	6.5	28
116	2019/11/04	22:43:32	-18.575	-175.272	10.0	6.6	7
117	2019/11/14	16:17:40	1.620	126.414	33.0	7.1	33
118	2019/11/23	12:11:15	1.644	132.815	5.0	6.2	24
119	2019/11/24	00:54:01	51.381	-175.511	20.0	6.3	6
120	2019/12/15	06:11:51	6.697	125.174	18.0	6.8	29
121	2020/01/19	16:58:20	-0.104	123.803	121.7	6.1	24
122	2020/01/23	05:53:02	51.984	-177.855	10.0	6.2	8
123	2020/02/05	18:12:37	-6.082	113.078	592.4	6.2	13
124	2020/02/09	06:04:29	-5.493	152.152	34.0	6.1	6
125	2020/03/17	16:06:22	-16.025	-172.191	10.0	6	3
126	2020/03/18	17:45:39	-11.052	115.138	20.7	6.2	25
127	2020/04/05	18:37:10	1.420	126.431	38.8	6	29
128	2020/05/02	12:51:06	34.205	25.712	17.0	6.6	41
129	2020/05/06	13:53:56	-6.795	129.861	107.0	6.8	62
130	2020/05/12	22:41:12	-12.066	166.648	107.0	6.6	48
131	2020/05/27	07:09:10	-17.157	167.864	10.0	6.1	5
132	2020/05/28	07:18:44	-22.236	-174.285	10.0	5.9	4
133	2020/05/28	09:46:57	-27.320	-175.370	12.0	5.8	22
134	2020/06/03	15:54:04	-7.006	116.928	639.9	5.7	3
135	2020/06/04	08:49:39	2.923	128.248	106.9	6.4	57
136	2020/06/07	20:06:38	-5.333	151.614	44.7	5.9	51
137	2020/06/18	12:49:53	-33.294	-177.838	10.0	7.4	55
138	2020/06/23	07:43:29	0.037	123.787	109.0	6	2
139	2020/06/25	21:05:18	35.595	82.416	10.0	6.3	38
140	2020/07/17	02:50:22	-7.839	147.775	73.0	7	57

Table S1. *(continued)*

No	date (yyyy/mm/dd)	time (hh:mm:ss)	lat (°N)	lon (°E)	dep (km)	M_W	N_s
141	2020/07/18	01:37:15	-10.410	161.394	48.0	5.8	5
142	2020/07/18	15:32:37	-15.246	-172.698	16.0	6.1	46
143	2020/07/21	20:56:29	-20.740	-178.690	626.0	6	17
144	2020/07/22	06:12:44	55.030	-158.522	28.0	7.8	56
145	2020/07/28	08:03:44	54.867	-161.144	41.3	6.1	7
146	2020/08/01	17:09:01	7.278	124.120	480.6	6.4	48
147	2020/08/01	19:22:05	-3.191	148.641	10.0	6.1	1
148	2020/08/02	09:29:57	-3.098	148.916	10.0	5.9	36
149	2020/08/05	12:05:36	-16.092	168.078	178.9	6.4	50
150	2020/08/18	22:23:59	-4.326	101.134	22.0	6.8	54
151	2020/08/21	04:09:52	-6.687	123.483	627.8	6.9	56
152	2020/10/01	01:13:36	-19.539	-174.122	28.0	6.4	56
153	2020/10/01	10:34:48	-6.087	148.658	109.2	6	55
154	2020/10/19	20:54:39	54.609	-159.652	31.1	7.6	59
155	2020/10/30	11:51:27	37.918	26.790	21.0	7	54
156	2020/11/15	22:37:46	8.590	126.560	54.5	6	56

Table S2. Local earthquakes used for surface-wave dispersion analysis. The event origin times, locations, focal depths, magnitudes (M_L), and numbers of stations (N_s) used for the analysis are presented.

No	date (yyyy/mm/dd)	time (hh:mm:ss)	lat (°N)	lon (°E)	dep (km)	M_L	N_s
1	2003/03/23	05:38:41	35	124.6	-	4.9	5
2	2003/03/30	20:10:53	37.8	123.7	-	5	4
3	2007/01/20	20:56:53	37.68	128.59	-	4.8	3
4	2013/05/18	07:02:02	37.68	124.63	11	4.9	
5	2014/04/01	04:48:35	36.95	124.5	8	5.1	5
6	2016/09/12	19:44:32	35.77	129.19	15	5.1	3
7	2016/09/12	20:32:54	35.76	129.19	15	5.8	3
8	2016/09/19	20:33:58	35.74	129.18	14	4.5	3
9	2017/11/15	14:29:31	36.11	129.37	7	5.4	3
10	2017/11/15	16:49:30	36.12	129.36	10	4.3	3
11	2018/02/11	05:03:03	36.08	129.33	14	4.6	10
12	2019/02/10	12:53:38	36.16	129.9	21	4.1	3
13	2019/04/19	11:16:43	37.88	129.54	32	4.3	4
14	2021/08/21	09:40:40	35.7	124.7	7	4	5

Table S3. Regional earthquakes used for surface-wave dispersion analysis. The event origin times, locations, focal depths, magnitudes (M_W), and numbers of stations (N_s) used for the analysis are presented.

No	date (yyyy/mm/dd)	time (hh:mm:ss)	lat (°N)	lon (°E)	dep (km)	M_W	N_s
1	2019/06/18	13:22:19	38.637	139.480	12.0	6.4	31
2	2019/06/24	00:11:44	34.930	140.018	43.7	5.3	32
3	2019/07/01	00:37:36	41.218	142.120	47.3	5.1	30
4	2019/07/11	21:21:57	23.892	122.874	15.7	5.0	32
5	2019/07/24	22:14:22	35.134	140.688	44.7	5.0	32
6	2019/07/29	20:37:42	32.845	140.554	52.9	5.7	19
7	2019/08/04	10:23:03	37.760	141.609	38.0	6.3	31
8	2019/08/07	21:28:03	24.477	121.933	20.7	5.8	32
9	2019/08/20	08:20:22	27.924	130.034	10.0	5.2	32
10	2019/08/24	04:52:46	37.334	142.501	11.6	5.1	32
11	2019/09/16	00:29:32	25.935	143.051	10.0	5.2	30
12	2019/10/05	20:18:19	27.991	128.116	10.0	5.1	28
13	2019/11/10	10:46:05	40.255	143.990	10.0	5.2	32
14	2019/11/29	04:01:40	39.162	143.017	19.0	5.4	32
15	2019/12/10	17:05:02	30.718	141.736	14.4	5.9	32
16	2019/12/11	09:39:08	37.759	141.836	38.2	5.2	29
17	2019/12/30	04:11:09	27.843	142.826	15.9	5.2	31

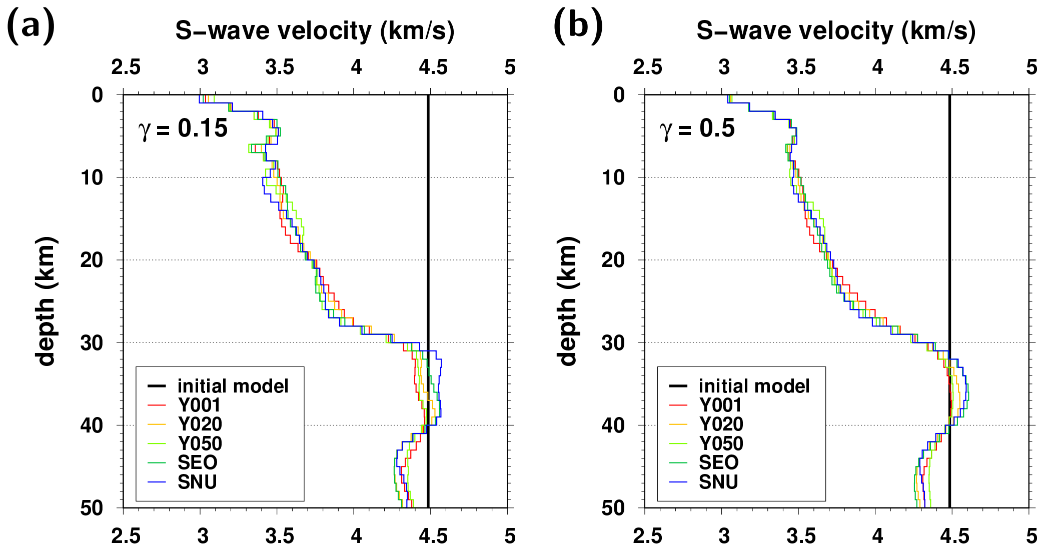

Figure S1. (a) Inverted models by joint inversion with influence factors (γ) of (a) 0.15 and (b) 0.5. A half-space homogenous model (solid line) is applied for the initial model in the joint inversion. Shear-wave velocity models for five stations (Y001, Y020, Y050, SEO, SNU) are inverted. The shear-wave velocity models are inverted stably for different influence factors and half-space homogenous model.

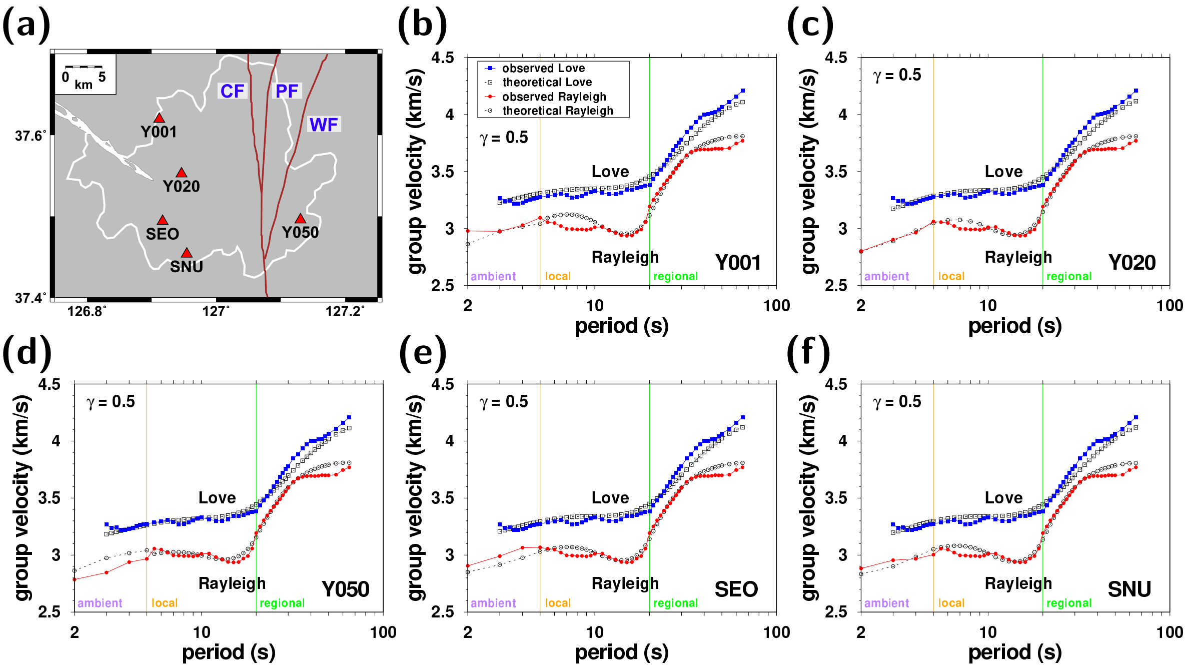

Figure S2. Surface-wave (Rayleigh, Love) dispersion curves by station: (a) map of stations, and surface-wave dispersion curves for stations (b) Y001, (c) Y020, (d) Y050, (e) SEO, and (f) SNU. Theoretical dispersion curves for the inverted velocity models from joint inversion with influence factor of 0.5 are compared with the reference observed surface-wave dispersion curves.

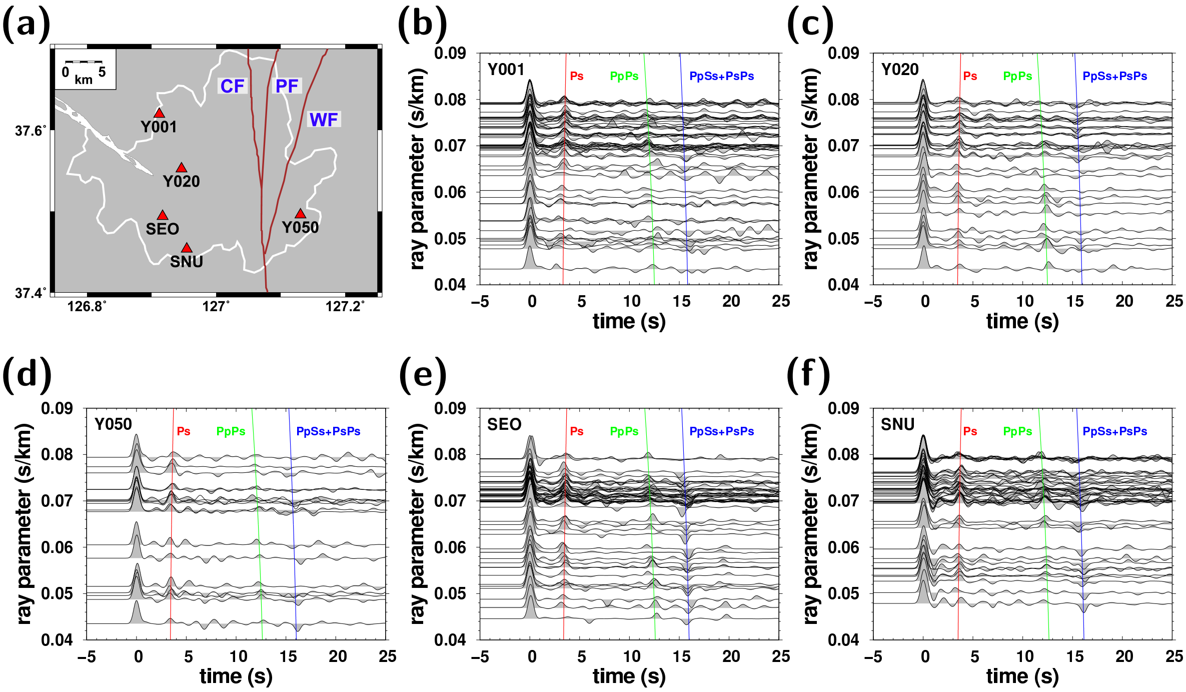

Figure S3. Receiver function profiles with Gaussian filter parameter of $\alpha_1 = 2.5$ as a function of ray parameter: (a) map of stations, and receiver function profiles at stations (b) Y001, (c) Y020, (d) Y050, (e) SEO, and (f) SNU. The observed receiver functions agree with the theoretical arrival times of Moho-converted phases (*Ps*, *PpPs*, *PsPs*+*PpSs*).

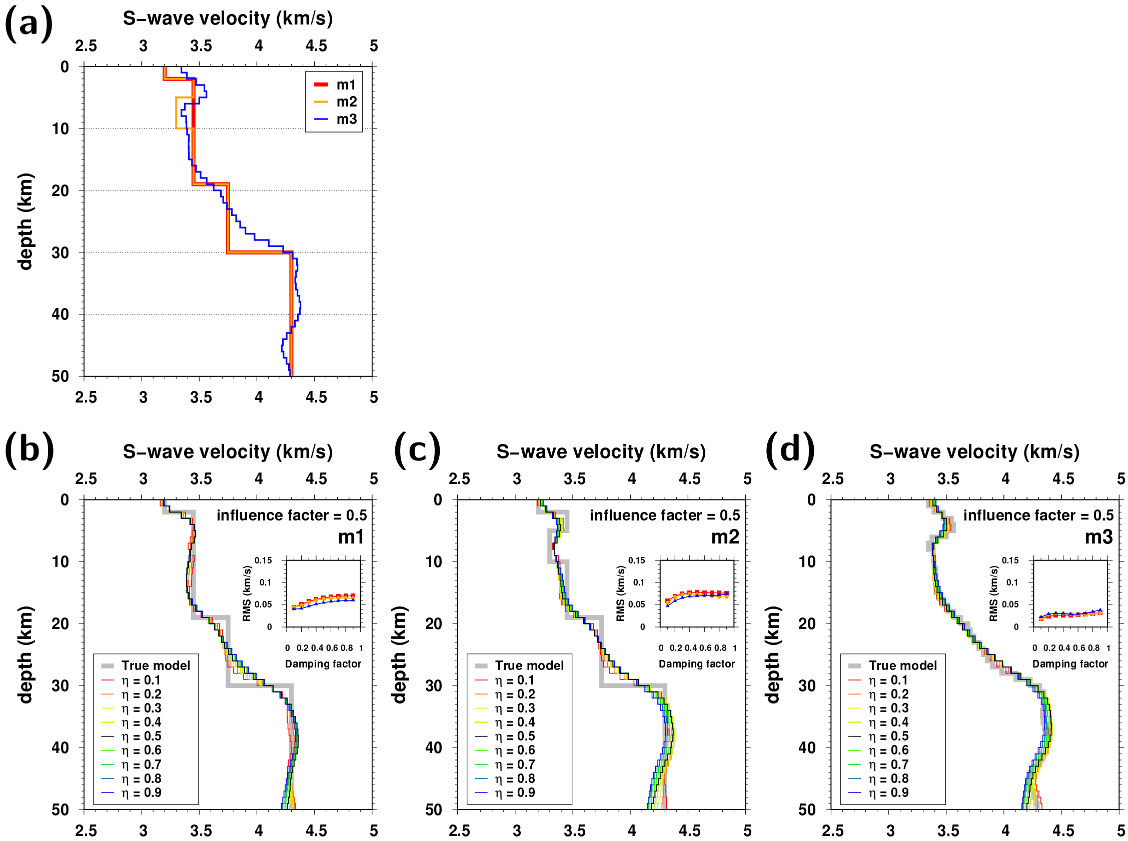

Figure S4. Synthetic tests of the joint inversion performance: (a) shear-wave velocity models (models m1, m2, m3), and inversion results with an influence factor of $\gamma = 0.5$ for input models (b) m1, (c) m2, and (d) m3. Inversions with influence factor of $\gamma = 0.5$ and damping factor of $\eta = 0.5$ yield relatively vertically smoothed models.

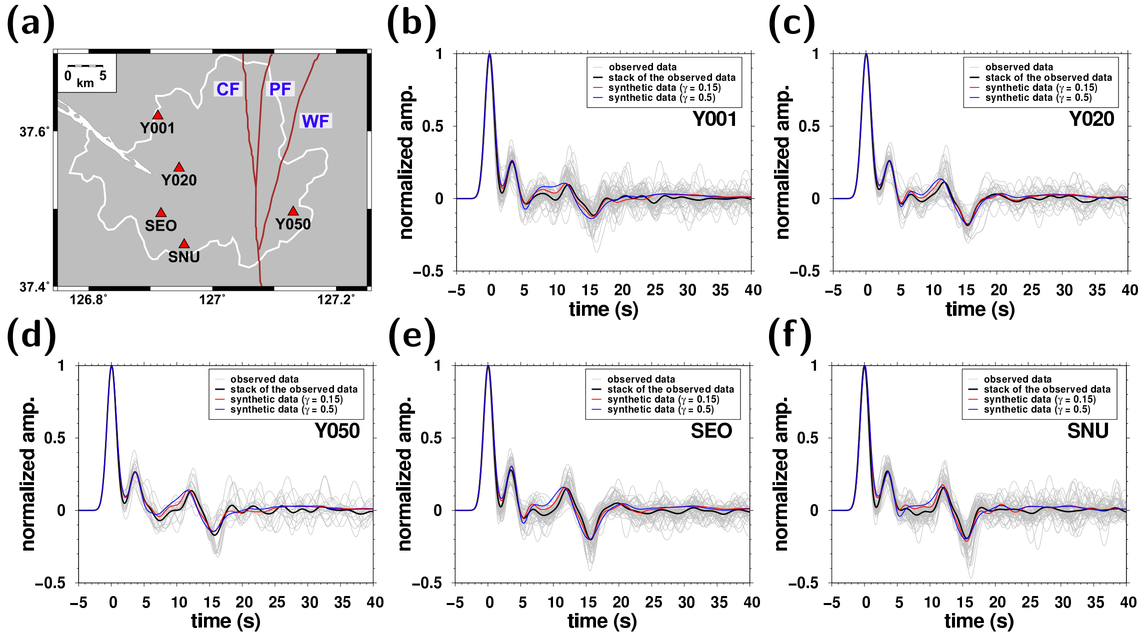

Figure S5. Comparison between observed and synthetic receiver functions for Gaussian filter parameter of $\alpha_1 = 1.0$: (a) map of stations, and receiver function profiles at stations (b) Y001, (c) Y020, (d) Y050, (e) SEO, and (f) SNU. Receiver function for every event is presented (thin lines). The observed receiver functions reasonably match with the synthetic receiver functions for influence factors of both 0.15 and 0.5.

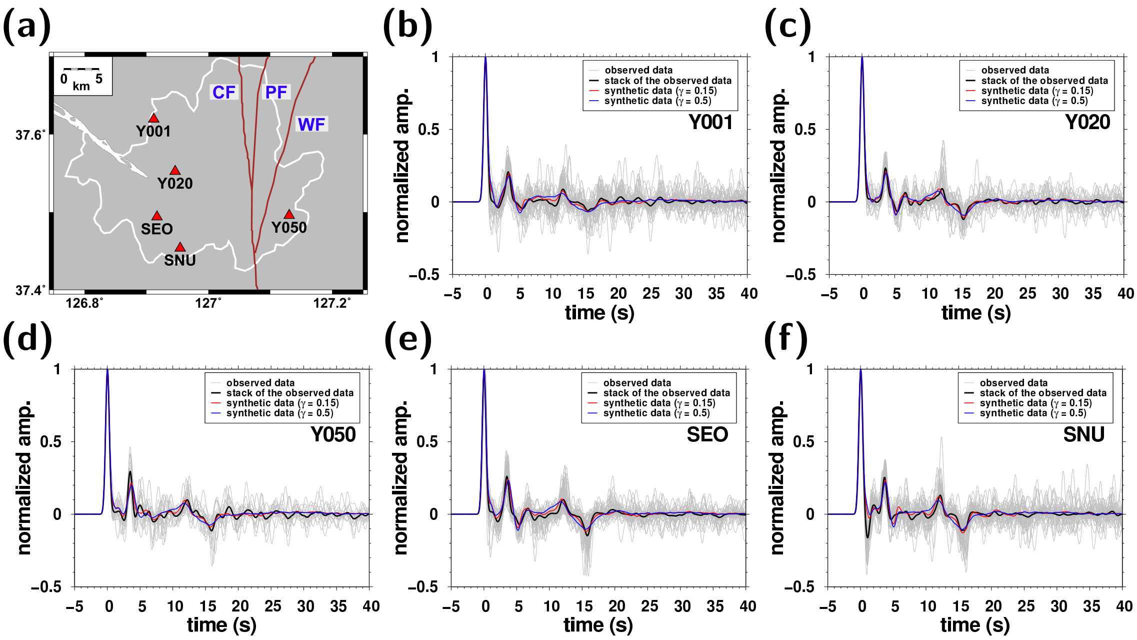

Figure S6. Comparison between observed and synthetic receiver functions for Gaussian filter parameter of $\alpha_1 = 2.5$: (a) map of stations, and receiver function profiles at stations (b) Y001, (c) Y020, (d) Y050, (e) SEO, and (f) SNU. Receiver function for every event is presented (thin lines). The observed receiver functions reasonably match with the synthetic receiver functions for influence factors of both 0.15 and 0.5.

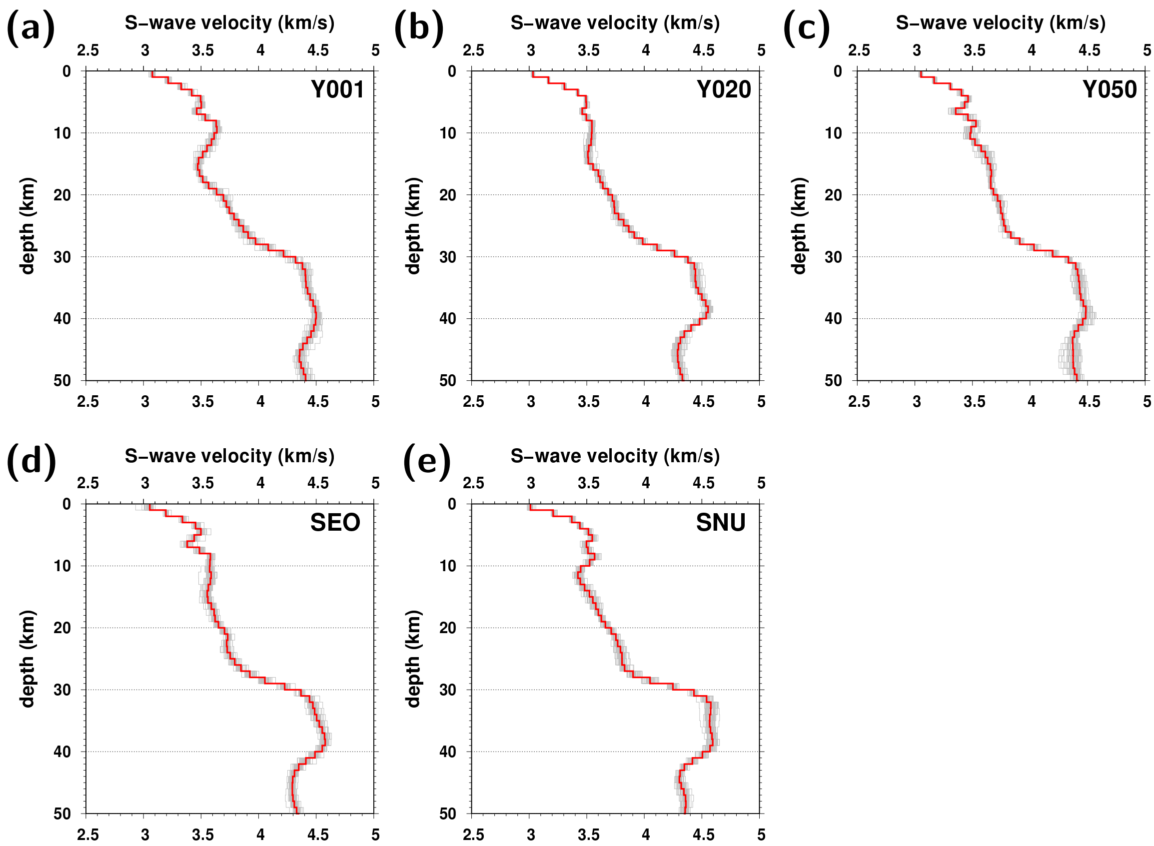

Figure S7. Bootstrap analysis of joint inversion for vertical velocity structures of media beneath stations (a) Y001, (b) Y020, (c) Y050, (d) SEO, and (e) SNU based on 11 data points. The velocity structures are inverted stably.

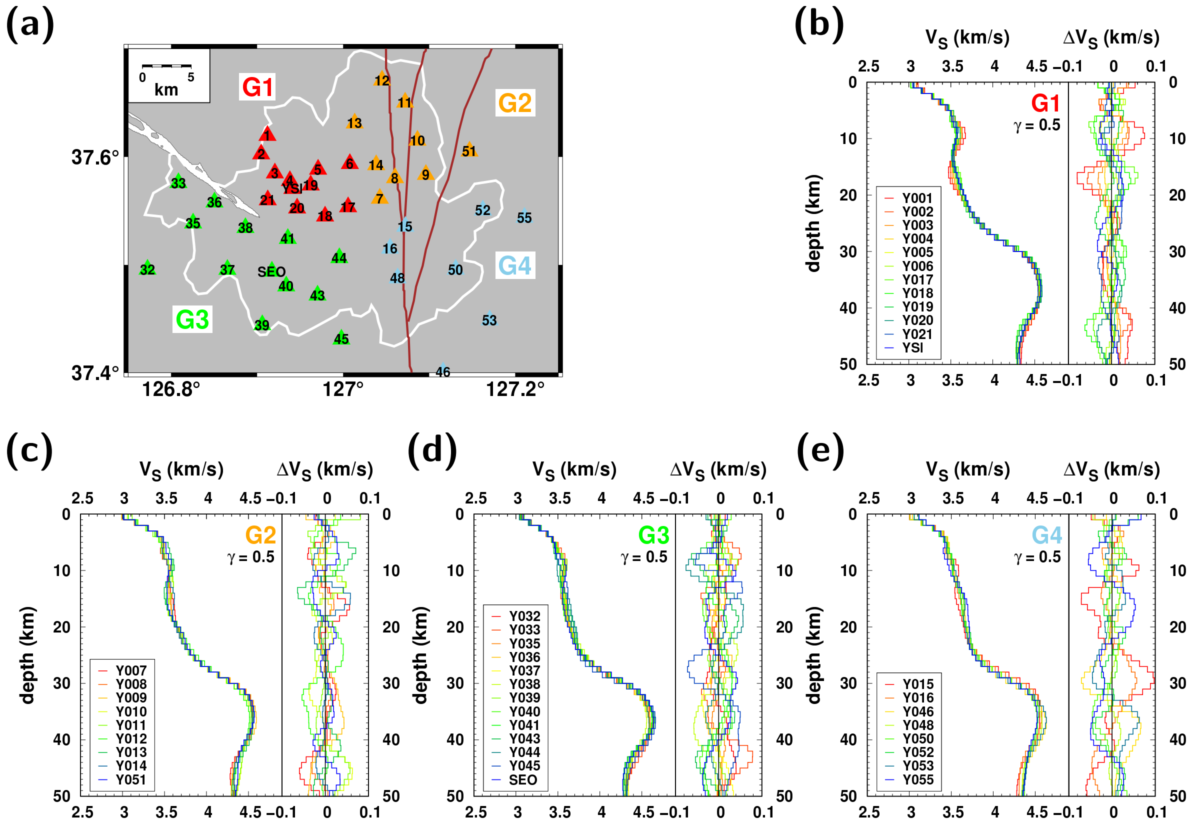

Figure S8. Comparisons of the vertical velocity structures for 4 subregions for joint inversion with influence factor of 0.5: (a) map of stations (triangles) in subregions (G1, G2, G3, G4) and fault traces (solid lines), and vertical velocity and differential velocity structures for subregions (b) G1, (c) G2, (d) G3, and (e) G4. The inverted vertical structures in subregions G1, G2, and G3 are similar and smoothed.

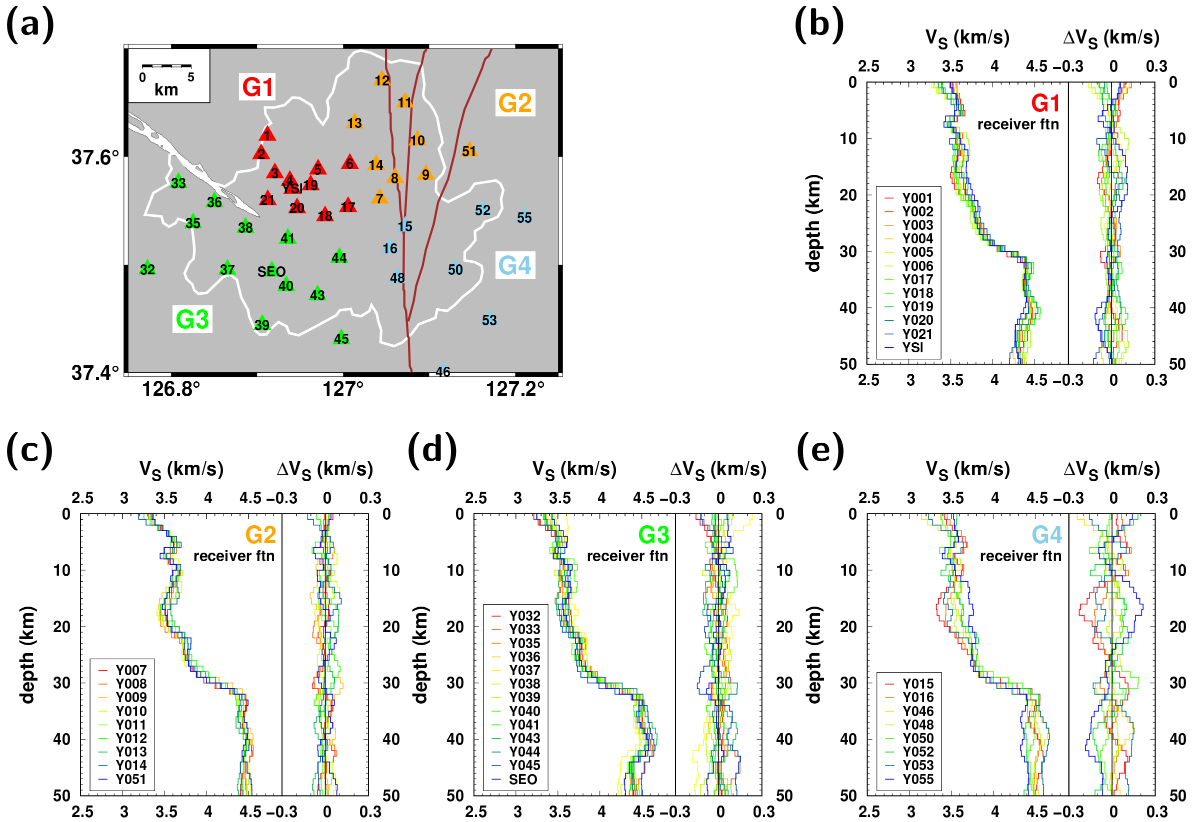

Figure S9. Comparisons of the vertical velocity structures for 4 subregions for conventional receiver function inversion: (a) map of stations (triangles) in subregions (G1, G2, G3, G4) and fault traces (solid lines), and vertical velocity and differential velocity structures for subregions (b) G1, (c) G2, (d) G3, and (e) G4. The inverted vertical structures in subregions G1, G2, and G3 relatively large differences.

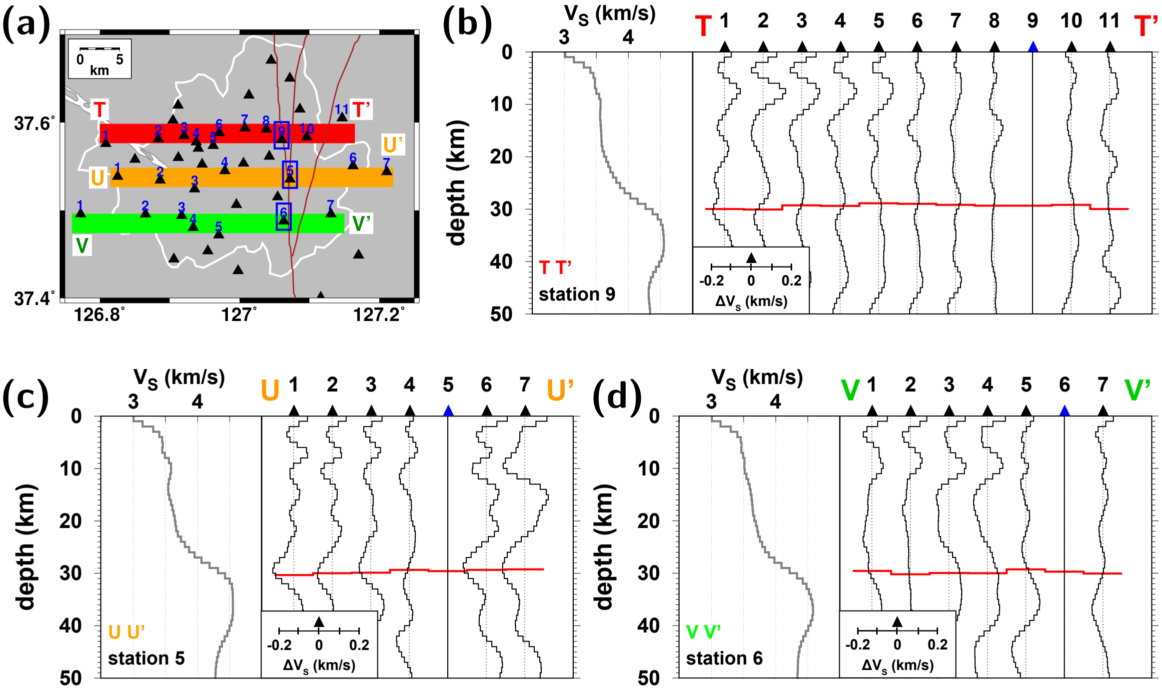

Figure S10. Comparison of inverted vertical shear-wave velocity and differential velocity structures for joint inversion with influence factor of 0.5: (a) map of stations (triangles) and three profiles (thick solid lines), and velocity models for profiles (b) TT' (c) UU' and (d) VV'. The profiles are placed across major faults (solid lines). The velocity structures of stations on the Chugaryeong fault are used for reference velocity models. The vertical and lateral variations in velocities are mild.

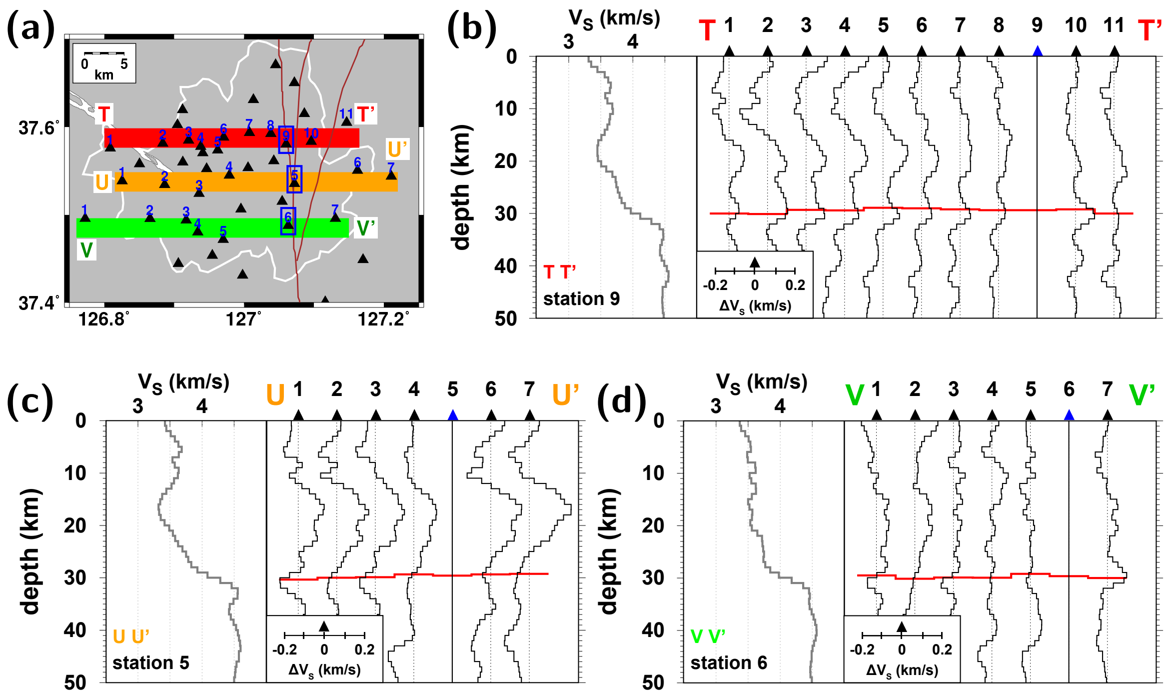

Figure S11. Comparison of inverted vertical shear-wave velocity and differential velocity structures for receiver function inversion: (a) map of stations (triangles) and three profiles (thick solid lines), and velocity models for profiles (b) TT' (c) UU' and (d) VV'. The profiles are placed across major faults (solid lines). The velocity structures of stations on the Chugaryeong fault are used for reference velocity models. The vertical and lateral variations in velocities are relatively large.

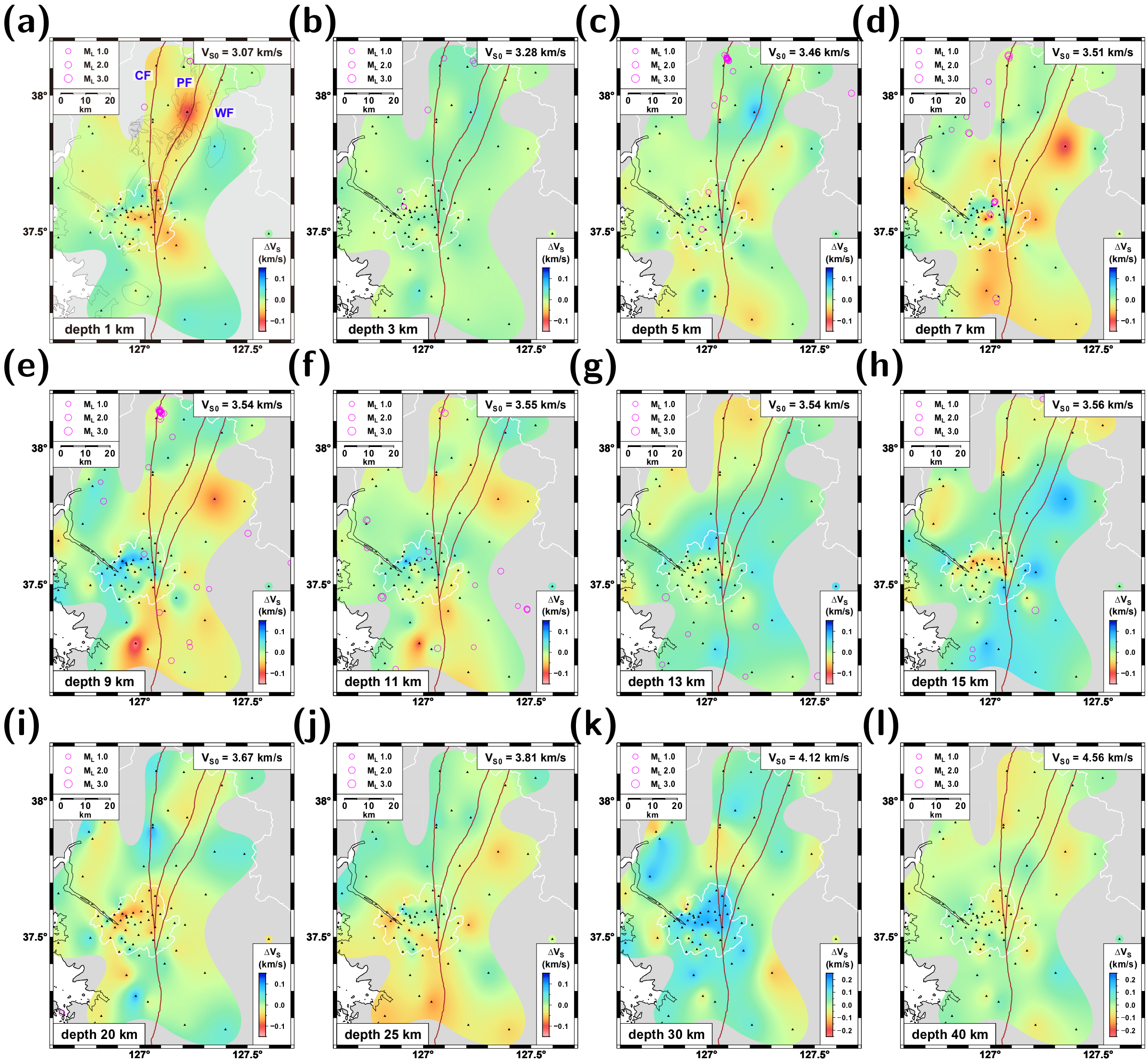

Figure S12. Shear-wave velocity models from joint inversion analysis with influence factor of 0.5 at depths of (a) 1, (b) 3, (c) 5, (d) 7, (e) 9, (f) 11, (g) 13, (h) 15, (i) 20, (j) 25, (k) 30, and (l) 40 km. The average velocities are denoted. The fault traces (solid lines), seismicity (circles), and stations (triangles) are marked. The lateral velocity variations are relatively mild.

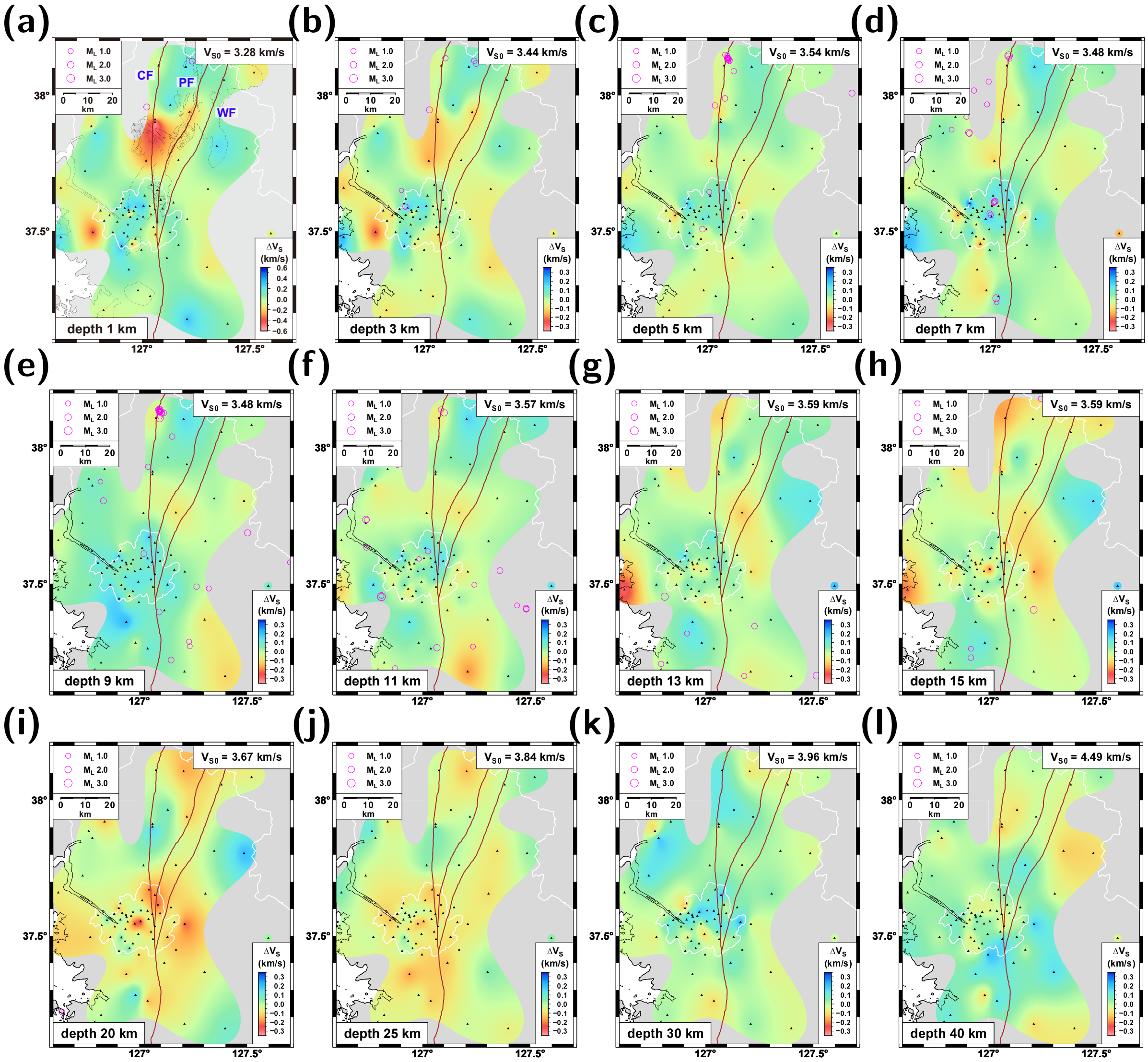

Figure S13. Shear-wave velocity models from receiver function inversion at depths of (a) 1, (b) 3, (c) 5, (d) 7, (e) 9, (f) 11, (g) 13, (h) 15, (i) 20, (j) 25, (k) 30, and (l) 40 km. The average velocities are denoted. The fault traces (solid lines), seismicity (circles), and stations (triangles) are marked. The lateral velocity variations are relatively large.

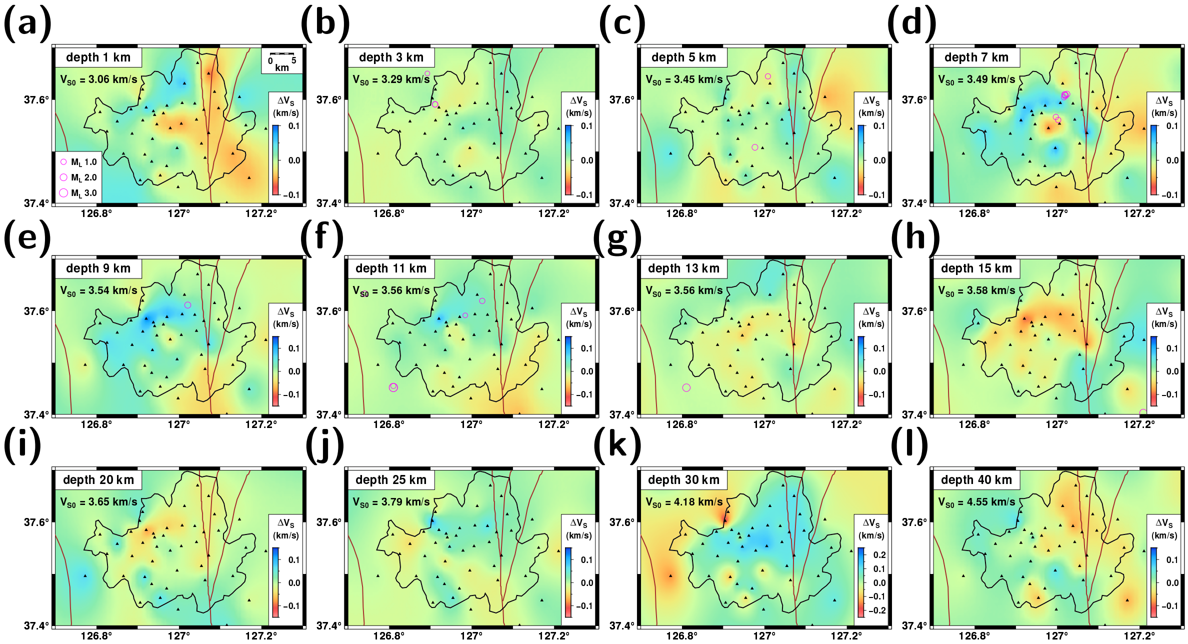

Figure S14. Enlarged views of the shear-wave velocity models from joint inversion analysis with influence factor of 0.5 for Seoul region at depths of (a) 1, (b) 3, (c) 5, (d) 7, (e) 9, (f) 11, (g) 13, (h) 15, (i) 20, (j) 25, (k) 30, and (l) 40 km. The average velocities are denoted. The fault traces (solid lines), seismicity (circles), and stations (triangles) are marked. The lateral velocity variations are relatively mild.

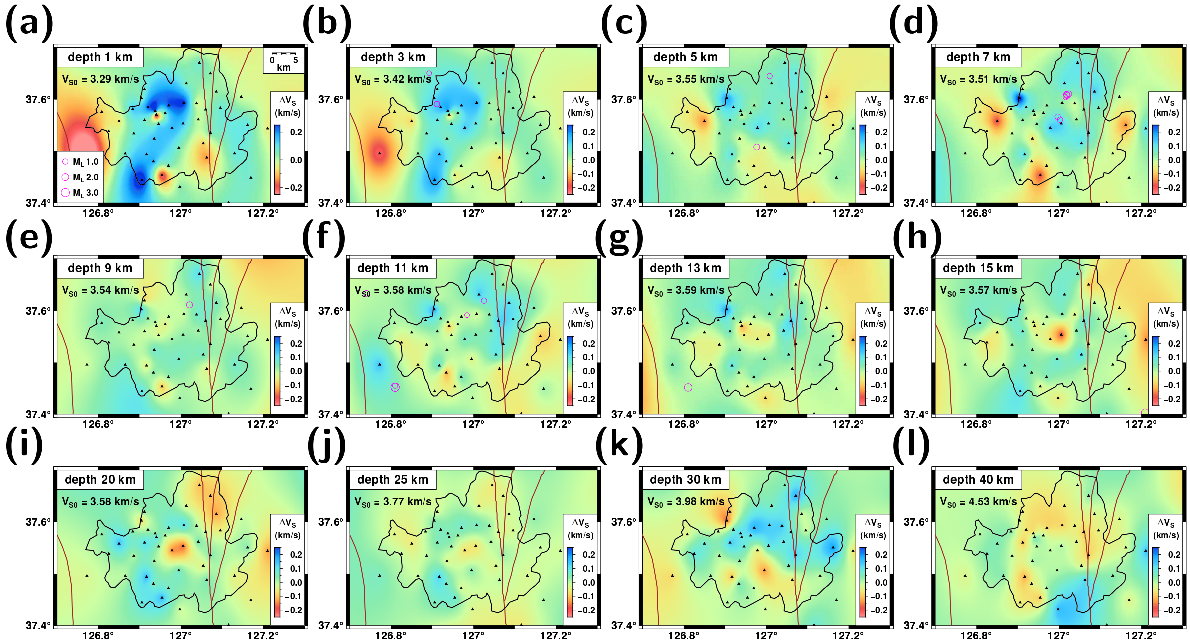

Figure S15. Enlarged views of the shear-wave velocity models from receiver function inversion for Seoul region at depths of (a) 1, (b) 3, (c) 5, (d) 7, (e) 9, (f) 11, (g) 13, (h) 15, (i) 20, (j) 25, (k) 30, and (l) 40 km. The average velocities are denoted. The fault traces (solid lines), seismicity (circles), and stations (triangles) are marked. The lateral velocity variations are relatively large.

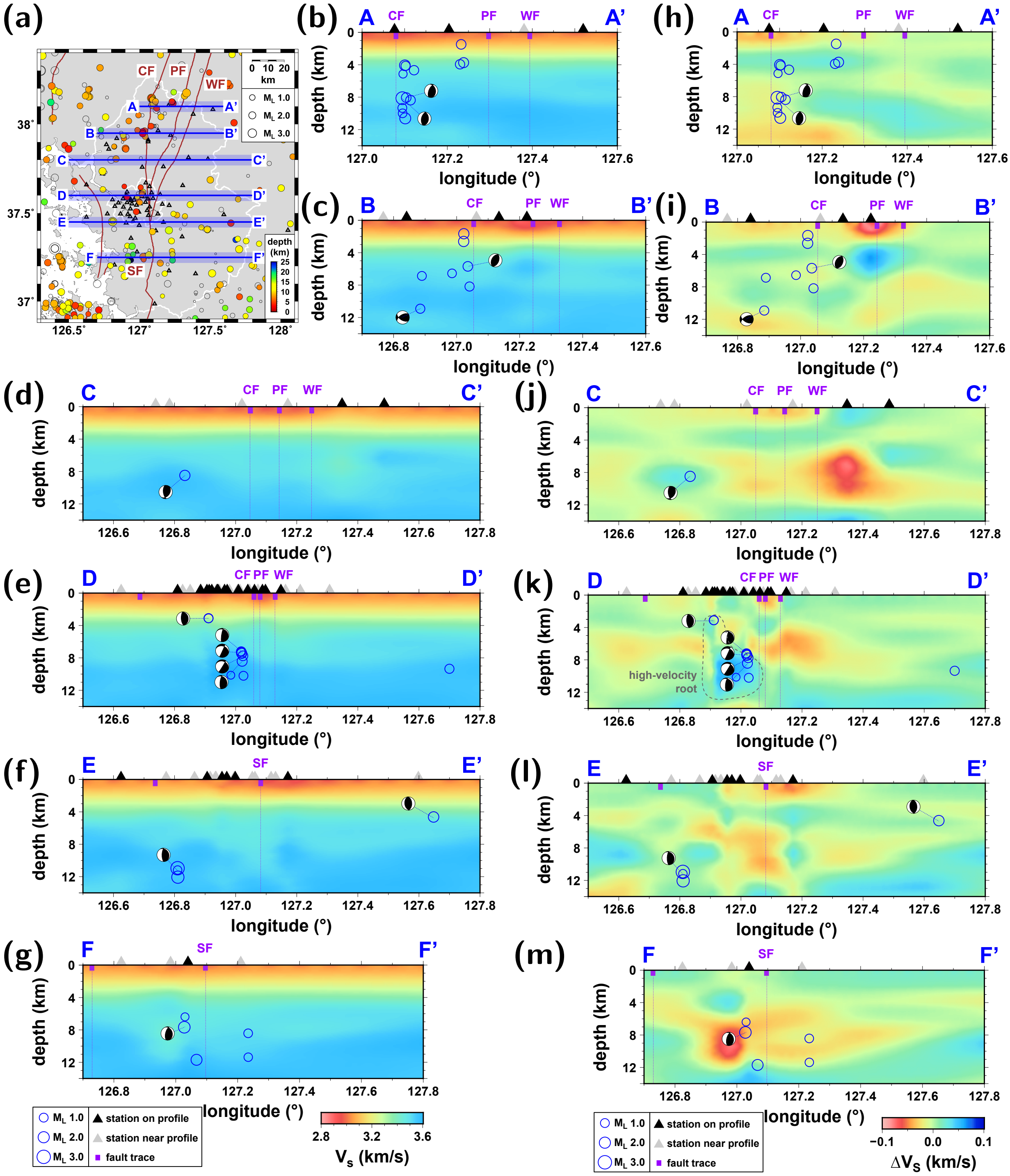

Figure S16. Upper-crustal shear-wave velocity and differential velocity structures for joint inversion with influence factor of 0.5: (a) map of profiles and stations, shear-wave velocity structures along profiles (b) AA', (c) BB', (d) CC', (e) DD', (f) EE', and (g) FF', and differential shear-wave velocity structures along profiles (h) AA', (i) BB', (j) CC', (k) DD', (l) EE', and (m) FF'. The seismicity and major fault traces are marked. The lateral velocity variations are relatively mild.

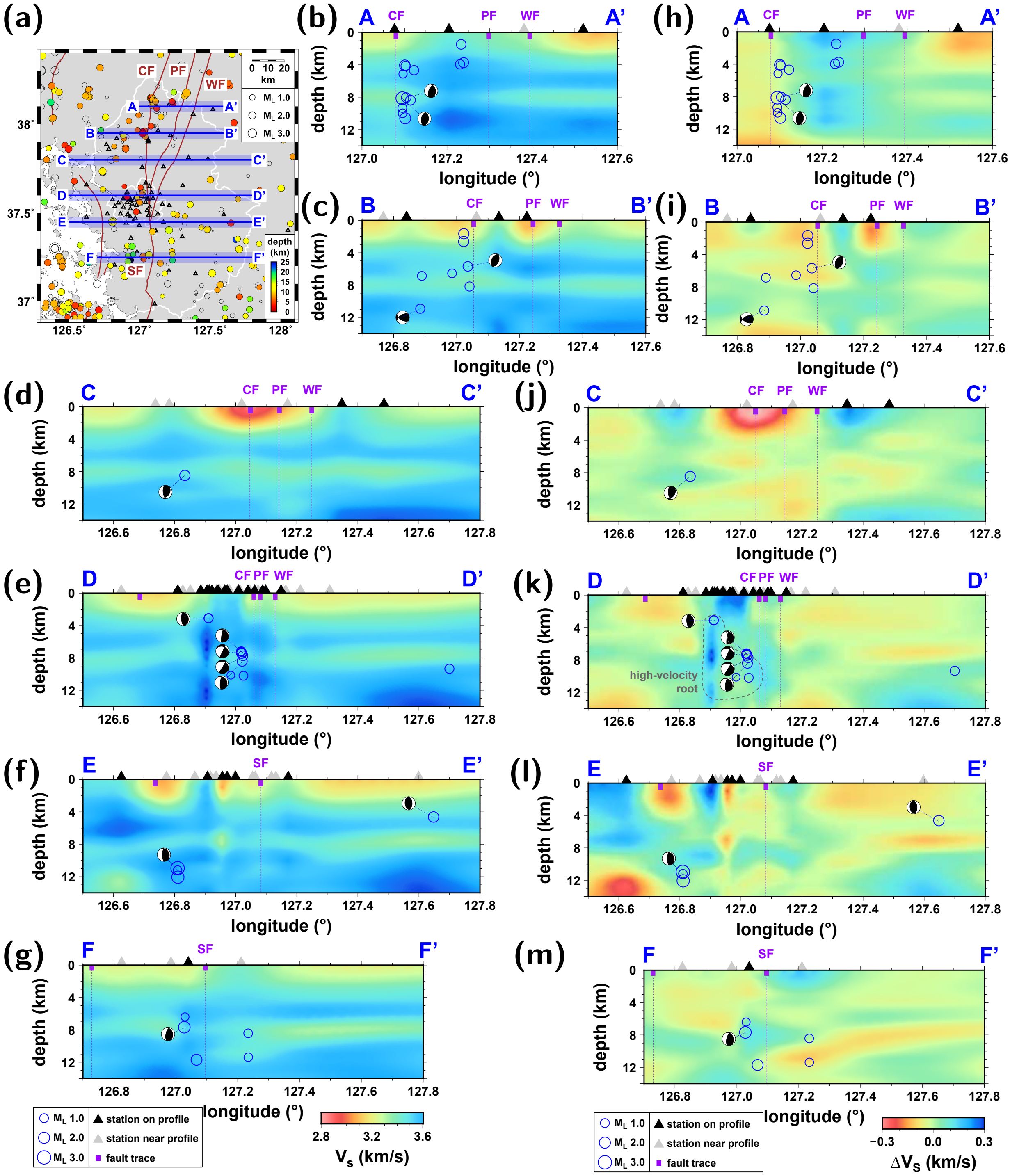

Figure S17. Upper-crustal shear-wave velocity and differential velocity structures for receiver function inversion: (a) map of profiles and stations, shear-wave velocity structures along profiles (b) AA', (c) BB', (d) CC', (e) DD', (f) EE', and (g) FF', and differential shear-wave velocity structures along profiles (h) AA', (i) BB', (j) CC', (k) DD', (l) EE', and (m) FF'. The seismicity and major fault traces are marked. The lateral velocity variations are relatively large.